DOI: 10.1478/AAPP.992A4

AAPP | Atti della Accademia Peloritana dei Pericolanti
Classe di Scienze Fisiche, Matematiche e Naturali
ISSN 1825-1242

Vol. 99, No. 2, A4 (2021)

GATE MONTE CARLO DOSIMETRY IN ^{90}Y TARE PLANNING: INFLUENCE OF SIMULATION PARAMETERS AND IMAGE RESAMPLING ON DOSIMETRIC ACCURACY AND OPTIMIZATION OF COMPUTATIONAL TIMES

DANIELE PISTONE [ab], ANTONIO ITALIANO [ab*], LUCREZIA AUDITORE [bc], ERNESTO AMATO [bc], ALFREDO CAMPENNÌ [cd] AND SERGIO BALDARI [cd]

ABSTRACT. Direct Monte Carlo (MC) simulation is considered the gold standard approach for internal dosimetry in nuclear medicine, and it is increasingly used in planning Trans-Arterial Radio-Embolization (TARE) of HepatoCellular Carcinoma (HCC) and hepatic metastases. However its computational times, longer with respect to other simplified approaches, constitute a limiting factor, especially when dealing with large size and finely discretized voxelized volumes. Aim of this work was the investigation of the influence of cuts on the production of secondary particles and of input CT images resamplings on dosimetric accuracy and computational time in patient-specific voxel-level MC simulations of ^{90}Y-labelled glass microspheres TARE treatment, to find optimal combinations of settings for speeding up such simulations. GATE GEANT4 interface was used to perform simulations employing CT and ^{99m}Tc SPECT as input data, examining multiple CT resolutions (via CT resamplings characterized by voxel volume factors 2, 8, and 64 with respect to native one, and a CT resampling with SPECT resolution) and production cuts (0.01 mm, 0.05 mm, 0.1 mm, 0.5 mm and some more, specific for each resampling). Increasing cut length and reducing CT resolution produces an early rapid decrease followed by a late slow decrease of simulation time as a function of this two parameters. A reduction up to 30% with respect to reference simulation time, while preserving acceptable dosimetric accuracy, was obtained. The best combination of settings among the examined ones resulted the choice of CT resampling with 8 times the native voxel volume and of 0.1-0.5 mm cut, ensuring dosimetric agreement within 1% in liver-related VOIs, while reducing simulation time to 45%.

1. Introduction

Three dimensional internal dosimetry is aquiring an increasingly important role in the optimization of Molecular RadioTherapy (MRT) treatments planning and monitoring (Strigari *et al.* 2014; Stokke *et al.* 2017). Notably in Trans-Arterial Radio-Embolization (TARE) therapy of HepatoCellular Carcinoma (HCC), strong interest is recently arising in personalized dosimetry (Chiesa *et al.* 2015; Garin *et al.* 2020), with a growing use of Monte Carlo (MC) method (Auditore *et al.* 2019, 2020; Milano *et al.* 2021). Direct MC

simulation of radiation emitted by radiopharmaceuticals and its interaction with living matter, employing functional and anatomic imaging as input data, is considered the gold standard dose evaluation approach for internal dosimetry (Tsougos *et al.* 2010; Dewaraja *et al.* 2012; Amato *et al.* 2018). In particular, the absorbed dose distribution in presence of relevant tissue inhomogeneities, such as at the interface between tissues of different density and composition (*e.g.*, lung - soft tissue, soft tissue - bone), and of strongly heterogeneous activity distributions, can be assessed accurately only by means of MC simulations (Auditore *et al.* 2019). In addition, the dose contribution from gamma-rays emitted at relevant distances from a target voxel is always adequately taken into account in MC, differently from other simplified and less computational demanding approaches, like voxel S-value and dose point-kernel convolution (Dewaraja *et al.* 2012). However, the high accuracy of MC evaluations is obtained with the drawback of requiring longer computational times with respect to other dosimetric approaches (Ai-dong *et al.* 2005; Ziegenhein *et al.* 2015; Huizing *et al.* 2018). Computational times can result a limiting factor especially when dose estimations on voxelized phantoms are carried out.

In this work we focused on voxelized MC internal dosimetry for ^{90}Y-labelled glass microspheres TARE treatment carried out based on pre-therapy ^{99m}Tc-labelled macroaggregated albumin (^{99m}Tc-MAA) SPECT and CT imaging data. The influence on dosimetric accuracy and on computational time introduced by the cuts on the production of secondary particles and by input of images with reduced resolution was investigated, with the aim of finding combinations of settings for optimizing the computational time without losing dosimetric accuracy. The study was conducted on a clinical case of ^{90}Y-TARE of HCC by means of GATE (Geant4 Application for Emission Tomography) (Jan *et al.* 2004), a simulation platform widely used in medical applications involving ionizing radiations (Sarrut *et al.* 2014), based on the well validated GEANT4 toolkit (Agostinelli *et al.* 2003; Amako *et al.* 2006). This work can be considered as a proof-of-concept for selecting optimal settings for MC voxel dosimetry in ^{90}Y TARE planning or retrospective studies.

2. Materials and methods

The pre-therapy clinical imaging data of a patient enrolled for ^{90}Y-labelled glass microspheres TARE of HCC were used as the starting point for the present dosimetric study. They consisted of an abdominal contrast-enhanced CT scan, for lesions localization, and an abdominal SPECT scan following the selective intra-arterial administration in liver of ^{99m}Tc-MAA, assumed to predict the therapeutic distribution of the ^{90}Y microspheres (Gnesin *et al.* 2016; Richetta *et al.* 2019) and to detect eventual pulmonary shunt. CT scan was performed with Siemens SOMATOM Definition AS and had a resolution of $512\times512\times146$ voxels, with voxel dimensions of $0.89\times0.89\times2.0$ mm^3. SPECT scan was performed with Philips BrightView Dual Head gamma camera and had a resolution of $128\times128\times105$ voxels, with voxel dimensions of $4.66\times4.66\times4.66$ mm^3. An axial view of the CT and SPECT images is shown in Figure 1a.

Resamplings of the native (N) CT image considered different voxel sizes, obtained by increasing the N CT voxel volume by a factor of 2, 8 and 64 (R2, R8, R64 hereafter), respectively. The CT resampling operation, performed with the 3D Slicer software (Kikinis *et al.* 2014; *3D Slicer Image Computing Platform* 2021), applied the `Resample Scalar`

`Volume` module using Lanczos interpolation (Moraes *et al.* 2019; *3D Slicer User Manual Documentation* 2021), leaving unchanged the overall volume of the native CT. Additionally, using the `Resample Image (BRAINS)` module by means of the Lanczos interpolation method, we resampled the N CT to match the image discretization of the SPECT scan (RS). The resolutions and voxel dimensions of the resampled CT images are reported in Table 1.

TABLE 1. Resolution and voxel dimensions of the CT image resamplings (R), compared to native (N) CT through voxel volume ratio v_R/v_N.

CT Name	v_R/v_N	Resolution	Voxel dimensions (mm^3)
N		512×512×146	0.89×0.89×2.00
R2	2.4	384×384×110	1.19×1.19×2.65
R8	8.0	256×256×73	1.79×1.79×4.00
R64	64.9	128×128×36	3.58×3.58×8.11
RS	63.4	128×128×105	4.66×4.66×4.66

Native and resampled CT images and the SPECT image were used as input data for GATE MC simulations, employing GATE version 9.0 (*GATE's Documentation* 2021) relying on GEANT4 version 10.05.p01 (*Geant4 Book for Application Developers* 2021; *Geant4 Physics Reference Manual* 2021). The CT images have been imported in GATE to generate voxelized phantoms reproducing patient's body morphology. `Automated Hounsfield Unit (HU) stoichiometric calibration` (*GATE's Documentation* 2021) was adopted to define materials and densities of phantom voxels. Through this procedure a material, *i.e.*, a chemical composition, is firstly assigned to each CT voxel on the basis of user defined HU intervals (Table 2). Then, HU sub-intervals of the aforementioned intervals are defined and a density is assigned to each of them through the interpolation of a HU-density calibration relation; in our study the bi-linear calibration relation (Schneider *et al.* 1996) of the employed CT scanner has been used. Therefore, a given HU interval corresponds to a defined material composition, whereas the several sub-intervals in it correspond to different densities of the same material. The sub-intervals are defined in such a way that densities differ from each other for a user defined value, that in our study was set 0.01 g/cm^3. Five intervals of HU, reported in Table 2, were set to identify the materials to be assigned, chosen from GEANT4 database (*Geant4 Physics Reference Manual* 2021) to properly reproduce the tissues composition and density inhomogeneities characterizing the thoraco-abdominal region of the human body. The SPECT scan was imported in GATE to define a voxelized source reproducing the radionuclide distribution, associating to each SPECT voxel a decay event probability through linear normalized conversion of its value. The starting position of the primary particles was randomly selected within source voxels, with uniform probability within each of them. The decay of the radionuclide, ^{90}Y, was simulated using `G4RadioactiveDecay` module, treating it as an ion type source, while the interactions of its daughters with the matter of the CT-derived phantoms were simulated through the `G4EmStandardPhysics_option3` physics list.

TABLE 2. HU intervals and corresponding density (ρ) intervals set for the assignment of materials (*Geant4 Physics Reference Manual* 2021) to phantom voxels.

Material	**HU interval**	**ρ (g/cm^3)**
G4_AIR	HU $\leq$ -855.7	$\rho \leq 0.10$
G4_LUNG_ICRP	$-855.7 <$ HU ≤ -126.5	$0.10 < \rho \leq 0.85$
G4_ADIPOSE_TISSUE_ICRP	$-126.5 <$ HU ≤ -38.9	$0.85 < \rho \leq 0.94$
G4_TISSUE_SOFT_ICRP	$-38.9 <$ HU ≤ 343.6	$0.94 < \rho \leq 1.2$
G4_BONE_CORTICAL_ICRP	HU > 343.6	$\rho > 1.2$

In GEANT4, charged particles could by default be tracked to the end of their range, but if all secondary particles were tracked infrared divergence would occur, since the differential cross sections of delta-electron production and bremsstrahlung grow rapidly when secondary energy decreases. The traditional solution to avoid that is to use production cuts for electrons, positrons, gamma (and protons if present), setting thresholds below which the production of further secondary particles is disabled and the residual energy is deposited locally (Allison *et al.* 2016; *Geant4 Book for Application Developers* 2021; *Geant4 Physics Reference Manual* 2021). The threshold cuts are set in terms of lengths, as range cuts, and are internally converted by the code into threshold energies for each material and for each particle type. The definition of a certain value of range cut has direct impact on the accuracy of spatial energy (and consequently dose) deposition. In the present study several simulations were performed for each phantom, adopting different values of production cuts on secondary particles production for electrons, positrons and photons: 0.01 mm, 0.05 mm, 0.1 mm, 0.5 mm. These values are smaller or even much smaller than the phantom voxel dimensions for all the resampling resolutions employed, ensuring in principle an accurate energy spatial sampling in all the cases. We moreover performed additional simulations adopting, depending on resampling resolution, a range cut of the order of voxel axial dimensions, to see the effect of using an - in principle - less accurate cut: 1.0 mm for N, 1.5 mm for R2, 2.0 mm for R8, 4.0 mm for R64 and RS. All the production range cuts used for the various CT resamplings are summarized in Table 3.

The absorbed doses and their statistical uncertainties δ (in terms of standard deviation of the mean, evaluated over the number of primary events (Sarrut *et al.* 2014)) were scored with GATE `DoseActor` employing the `MassWeighting` algorithm, with voxel resolutions equal to the ones of the phantom used each time, respectively. To deduce the correct 3D absorbed dose maps, the absorbed dose value inside each voxel of the MC output dose maps, D^{out}_{ijk}, was divided for the number of primary events simulated, N_{evts}, and multiplied for the cumulated activity, $\tilde{A}$:

$$D_{ijk} = \frac{D^{\text{out}}_{ijk}}{N_{evts}} \cdot \tilde{A} \tag{1}$$

$\tilde{A}$ was calculated analytically in the reasonable assumptions, for TARE treatments, of instantaneous uptake and of physical-only mono-exponential decay, following from absence

TABLE 3. Production range cuts on secondary particles used in simulations for the different CT resamplings employed.

Production cut (mm)	**CT**				
	N	R2	R8	R64	RS
0.01	✓	✓	✓	✓	✓
0.05	✓	✓	✓	✓	✓
0.1	✓	✓	✓	✓	✓
0.5	✓	✓	✓	✓	✓
1.0	✓				
1.5		✓			
2.0			✓		
4.0				✓	✓

of biological clearance:

$$\tilde{A} = A(0) \int_0^{\infty} \exp(-t/\tau_{^{90}Y}) dt = A(0) \cdot \tau_{^{90}Y} \tag{2}$$

where $\tau_{^{90}\mathrm{Y}}$ is the exponential time constant of ^{90}Y ($\simeq 332916$ s) and A(0) is the administered activity to the patient (2.49 GBq).

Segmentations were performed to define Volumes Of Interest (VOI) corresponding to the following organs or organ regions: liver, lesions, liver perfused, healthy liver, healthy liver perfused, right and left kidney, right and left lungs. Liver, lesions and kidneys were manually segmented on the native CT; lungs (actually the lower part of the lungs, visible in the CT field of view) were segmented on native CT using a thresholding method, selecting only the CT voxels with HU < -130; liver perfused was segmented on the SPECT setting a threshold at 5% of the maximum SPECT value within liver; healthy liver was obtained by logical subtraction of lesions from liver, while healthy liver perfused by by logical subtraction of lesions from liver perfused. In Figure 1 are shown axial projections of the VOIs representing liver-related regions and lungs.

3D Slicer was used to evaluate average doses $\langle D \rangle$ and Dose Volume Histograms (DVHs) inside the defined VOIs, using `Segment Statistics` module and *Dose Volume Histogram* module, respectively. When dose map resolution is different from the resolution of a VOI segmentation, 3D Slicer performs an automated adaptation of the segment voxels to the image on which they are applied for calculations. Volumes of all the employed VOIs, including adapted ones, are reported in the Annex (Table A1). Each $\langle D \rangle$ was obtained averaging the N_W^{vox} values of dose of the voxels included in the W-th VOI:

$$\langle D \rangle = \frac{\sum_{i,j,k \in W} D_{ijk}}{N_W^{vox}} \tag{3}$$

For each average dose, the associated average statistical uncertainty $\langle\delta\rangle$ for the voxels of the considered VOI was calculated. In addition, the average of the statistical uncertainties in VOIs over the production cuts, *i.e.*, averaging between simulations employing CTs with same resolution, was evaluated, and it is hereafter referred to as Δ:

$$\Delta = \frac{\sum_C \langle\delta\rangle_C}{N_C} \tag{4}$$

where C indicates the production cut and N_C indicates the number of different production cuts for each CT resolution employed. Average doses for the various resamplings (Table 1) and production cuts (Table 3) have been compared in terms of relative percent differences ε (%), taking the average dose coming from the simulation employing the native CT phantom and the thinner cut (0.01 mm) as a reference ($\langle D\rangle_{ref}$):

$$\varepsilon = 100 \cdot \frac{\langle D\rangle - \langle D\rangle_{ref}}{\langle D\rangle_{ref}} \tag{5}$$

DVHs - histograms representing the fraction of volume (υ) of a given VOI receiving at least a given amount of absorbed dose - were compared with the reference simulation one in terms of relative per cent difference σ between volume percentages, evaluated "dose bin by dose bin" (with a binning equal to 0.2 Gy for all the DVHs):

$$\sigma = 100 \cdot \frac{\upsilon - \upsilon_{ref}}{\upsilon_{ref}} \tag{6}$$

In each simulation, we employed $2{\cdot}10^8$ primary events (N_{evts}) to guarantee an average dose statistical uncertainty below 3% in lesions, below 4% in liver perfused and below 5% in healthy liver perfused, for the reference simulation. Each simulation was run individually in a single processor and without other other concomitant processes in order to have the same CPU and RAM conditions for all the simulations. Simulations run on an Intel® Xeon® PC with CPU E5-2620 v4 @ 2.10GHz processors. Simulation times, expressed in terms of the GATE variable `ElapsedTimeWoInit`, were recorded for each simulation, and the ratios with respect to the simulation time of the reference simulation were calculated.

3. Results and discussion

Figure 1b shows an axial view of the dose map obtained from reference simulation - employing native CT and 0.01 mm production cut - , fused with native CT image. In Figure 2 and Figure 3 are reported in histogram form the average absorbed doses $\langle D\rangle$ in the defined VOIs, referring to liver and to lungs and kidneys, respectively, together with the relative percent differences ε with respect to the reference simulation. $\langle D\rangle$'s and ε's are also reported in Tables A2-A6 in the Annex, including average statistical uncertainties $\langle\delta\rangle$ on doses.

$\langle D\rangle$'s in all the five liver-related VOIs, obtained with all the resamplings except for R64 (and RS in the case of healthy liver), show an agreement with reference simulation within 1% in terms of ε, independently from the production cuts. In the case of R64 resampling, $\langle D\rangle$'s show ε's within 6% for all liver VOIs independently form cuts. For RS resampling,

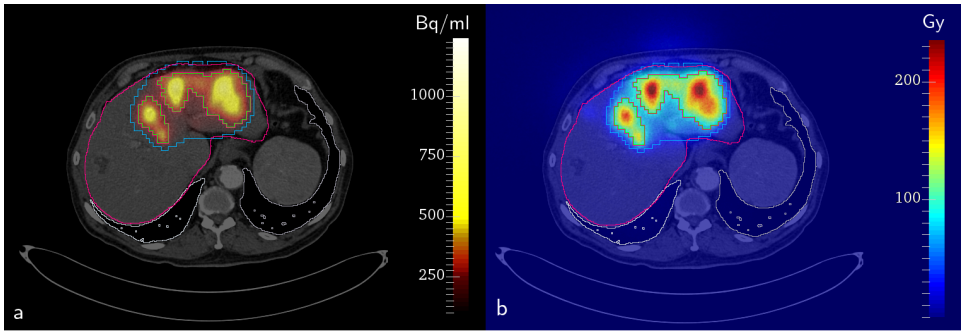

FIGURE 1. Axial slice of the fusion image of native CT and SPECT (a) and the corresponding slice showing fusion of native CT and dose map obtained from reference simulation (b); in both figures the VOI segmentations of liver and lungs used in this work are also shown: lesions in green, liver perfused in light blue, healthy liver in magenta, lungs in grey.

$\langle D \rangle$'s in healty liver VOI show ε's within 4% for all the cuts. Considering a fixed resampling, no appreciable differences in average doses are observed in liver-related VOIs varying the production cuts, even in the case of cuts having dimensions comparable with the ones of voxels. $\langle D \rangle$'s in lung VOIs exhibit agreement with reference within 5% for R2 and R8 resamplings, within 13% for R64 and RS resamplings, irrespective of production cuts. $\langle D \rangle$'s in kidney VOIs show ε's within 4% for R64 resampling and within 2% for all the other resamplings, with only minimal differences when varying the productions cuts. Overall, the highest differences ε's are observed in the case of R64 resampling, compared to the other resamplings, including RS which has a comparabale voxel size. This can be partly ascribed to the resulting volumes of the VOIs on the resampled images, which exhibit the larger differences for the R64 resampling, of the order of 1% for liver-related VOIs, as shown in Table A1 of the Annex (while for all the other resamplings, the differences in liver-related VOI volumes are well below 0.5%).

DVHs and relative percent differences σ with respect to reference simulation DVH are reported in the Annex, in Figures A1-A12. DVHs for liver-related VOIs show an excellent agreement in a wide range of dose values, from zero to 200-300 Gy, depending on the resampling adopted, with fluctuations affecting, in general, only high values of dose, corresponding to volume percentages below 1%; σ in healthy liver perfused VOI shows some fluctuations at lower dose values for R8, R64 and RS resamplings. DVHs referring to lung and kidney VOIs show good agreement too, considering the dose intervals in which they show significative volume percentages, with fluctuations in σ starting to widen in correspondence of the lower part of the tails of DVHs. No significative differences in DVHs and σ's are observed varying the production cuts for a fixed resampling.

Concerning voxel level statistical uncertanties on dose estimates, considering a fixed resampling, $\langle \delta \rangle$'s do not show significant differences varying the production cuts. Instead, varying the resampling, and consequently the voxel volumes, $\langle \delta \rangle$'s rapidly decrease with increasing the voxel volume. This behaviour is understandable considering that δ's are standard deviations of the mean evaluated on the number of primary events. Therefore,

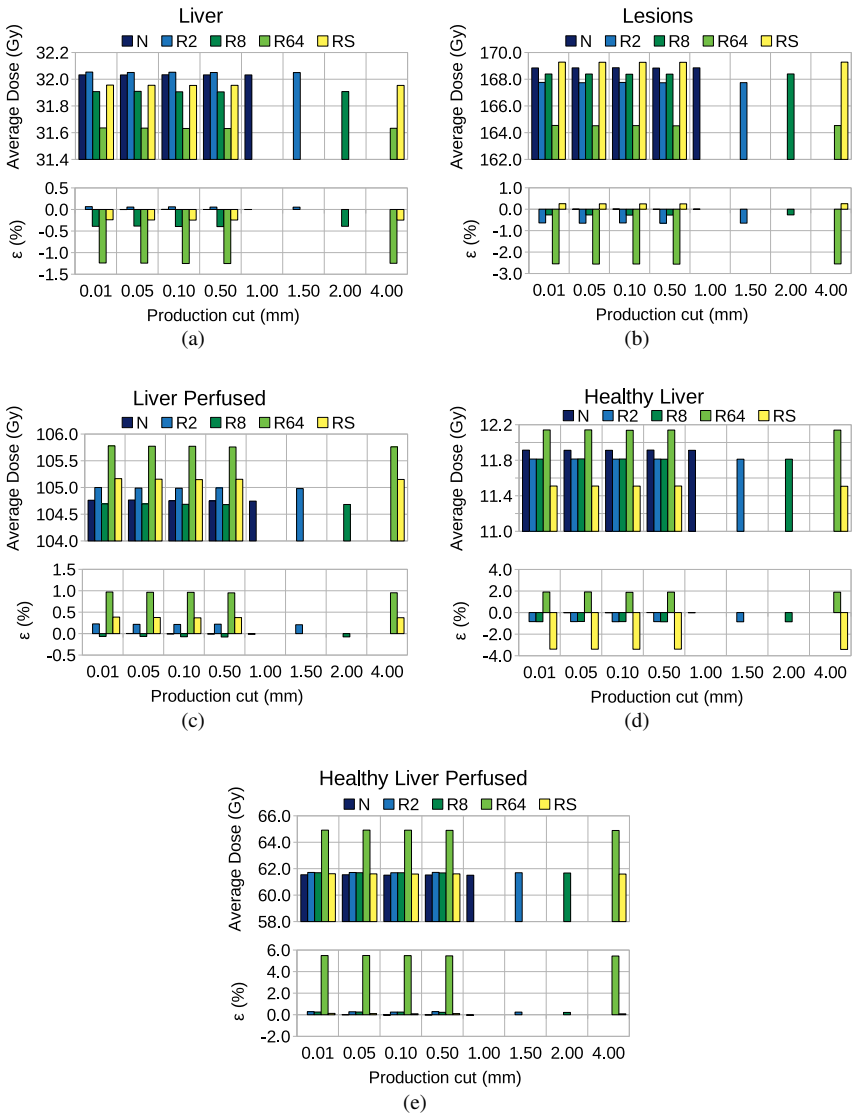

FIGURE 2. $\langle D \rangle$ and ε in the VOIs referring to liver, for all the production cuts and CT resampling volumes used (N, R2, R8, R64, RS, as indicated in Table 1, denoted with different colors).

leaving equal the number of primary events but increasing the size of the volume in which doses are scored (the voxels in our case), more dose depositions are expected to be sampled in a single larger volume rather than in multiple smaller volumes. Consequently the estimate

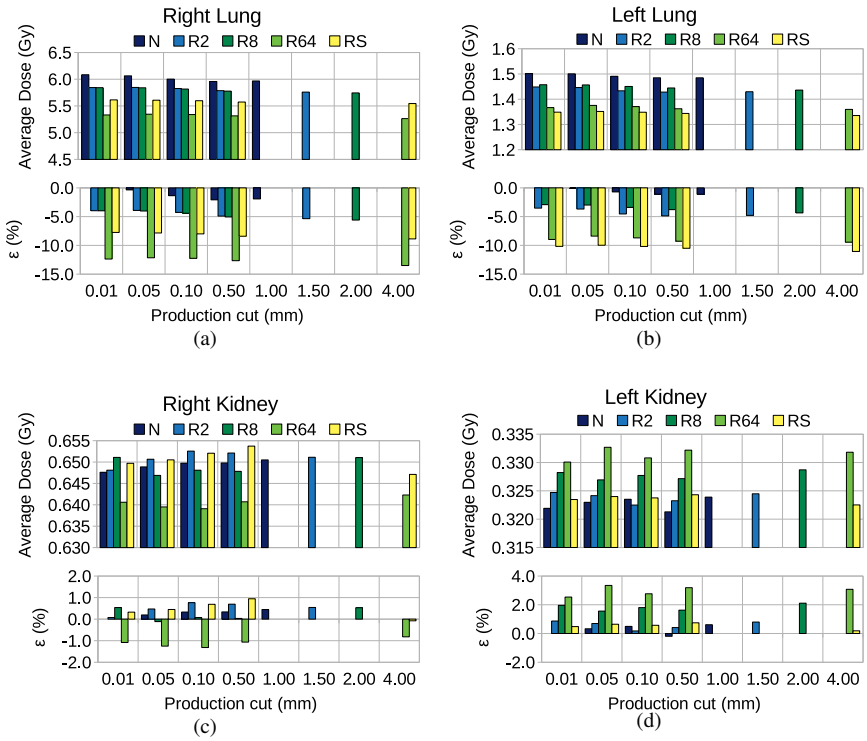

FIGURE 3. $\langle D \rangle$ and ε in the VOIs referring to lungs and kidneys, for all the production cuts and CT resampling volumes used (N, R2, R8, R64, RS, as indicated in Table 1, denoted with different colors).

of the total dose or of the average dose in a larger volume tends to have lower standard deviation with respect to the ones of the smaller volumes taken singularly.

In Figure 4 are shown the Δ's (Eq. 4) in all the VOIs considered in this study as a function of voxel volume ratio with respect to native CT. Considering the Δ values corresponding to N CT and to resamplings R2, R8 and R64, which conserve the total volume of the CT, their trend as a function of voxel volume ratio is well described by a bi-exponential function of the form $f(x) = ae^{-bx} + ce^{-dx}$. Δ's for the RS resampling, having similar voxel volume to R64 resampling but with different total volume of the CT, do not differ much from R64 values, and consequently they neither depart from the described trend as a function of voxel volume ratio. It should be noted that the described decrease of uncertainty with increasing voxel volume concerns only statistical uncertainty of MC estimates, and the reported trends do not take into account systematic uncertainties coming from the resampling procedure applied on CT, whose evaluation is beyond the scope of this work.

In Figure 5 are reported the simulation time ratios with respect to the reference simulation for all the simulations performed, as a function of production cut length in panel (a) and as a function of voxel volume ratio with respect to reference simulation in panel (b); the

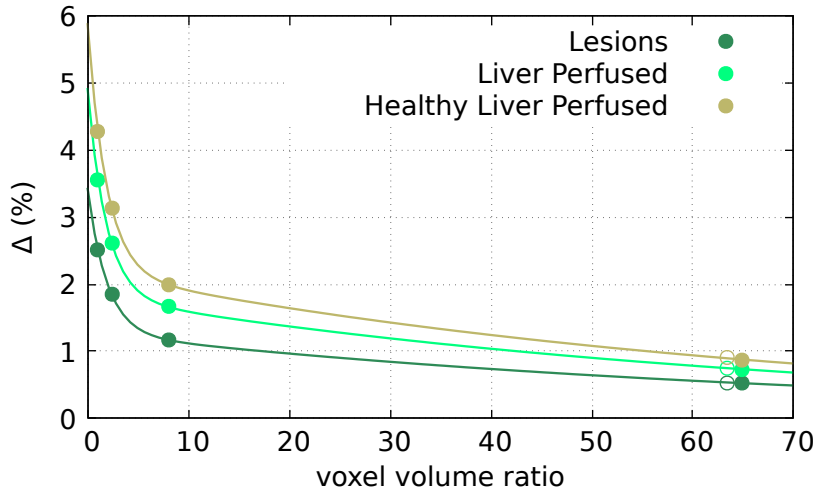

(a)

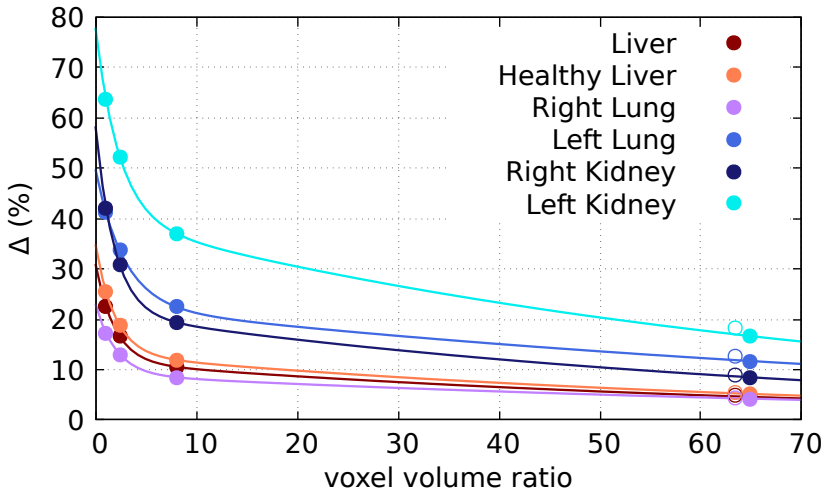

(b)

FIGURE 4. Δ values in VOIs as a function of voxel volume ratio with respect to N voxel volume. Full circles refer to simulations employing N, R2, R8 and R64 CTs, fitted with bi-exponential function; open circles refer to simulations employing RS CT, not considered in the fits but depicted for completeness.

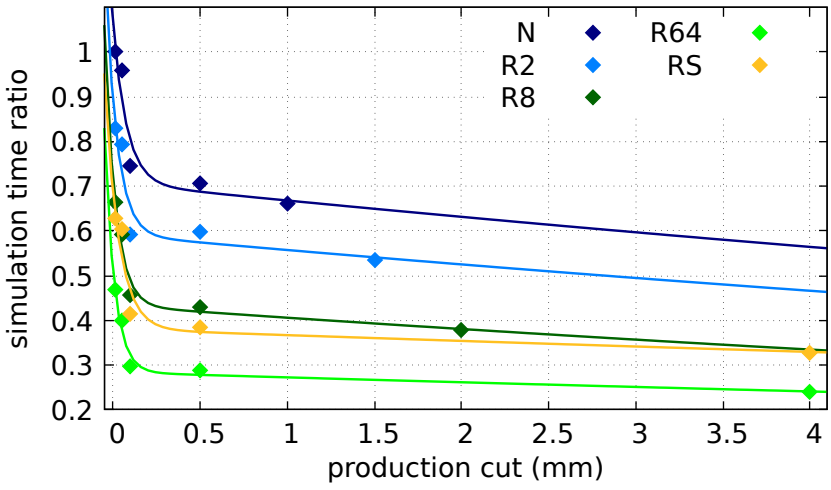

(a)

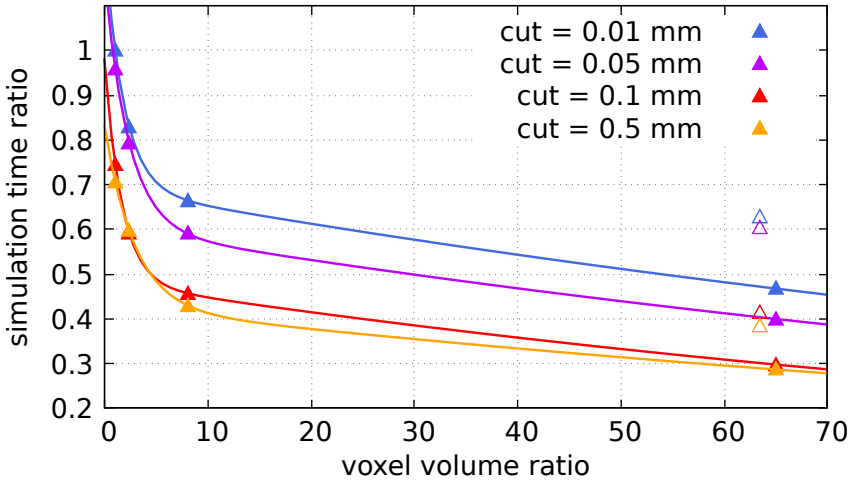

(b)

FIGURE 5. Simulation time ratios with respect to the reference simulation time (which lasted 139.5 h), as a function of production cut lenght (a) and of voxel volume ratio (b). Full triangles in (b) represent simulations using N, R2, R8 and R64 CTs, taken into account for fits; open triangles represent simulations using RS CT, not considered for fits.

reference simulation lasted 139.5 hours. For all the CT used, increasing the length of production cuts up to about 0.1 mm causes a rapid decrease of simulation time, while for higher cuts the decrease continues with lower slope. For each CT the behaviour as a function of production cut length is well approximated by a bi-exponential function with an early rapid decay term and a subsequent slow decay term. Given a CT resolution, using cuts equal or larger than 0.1 mm, among the ones examined in this work, leads to a decrease of simulation time by about 25-35% with respect to the cases with the smallest cut used (0.01 mm).

Considering a fixed production cut, by increasing the voxel size through CT resamplings conserving the total volume of the CT, as done with R2, R8 and R64 resamplings, a bi-exponential decrease of simulation times is observed. For each fixed cut, a reduction of simulation time by about 17%, 35% and 60% with respect to simulations using native CT is obtained with simulations using R2, R8 and R64 resamplings, respectively. In the case of RS resampling, not conserving the total volume of the CT, despite having a similar voxel volume to R64 resampling, simulation times result higher, comparable instead with the ones of R8 resampling. Therefore RS results do not follow the bi-exponential trend described for N, R2, R8 and R64, as visible in Figure 5b looking at the open triangles.

Taking into account the behaviour as a function of the examined parameters (voxel volume via CT resampling and secondary production cuts) of average dose relative percent differences ε, as an index of accuracy of the dose evaluation, together with the simulation time ratios, as an index of computational time optimization, it appears that the optimal combination of parameters is R8 resampling - which doubles voxel side - with 0.1 mm cuts. This combination ensures agreement within 1% in terms of ε in liver-related VOIs, within 4% in lungs and within 2% in kidneys (which by the way are not generally considered in TARE dosimetry), while reducing the simulation time to less than half of the reference simulation time. 0.5 mm cut does not alter significantly the accuracy in terms of ε and can be equally used, but the benefit in terms of simulation time ratio is also minimal (from $\sim$47% with 0.1 mm cut to to $\sim$42% with 0.5 mm). 2.0 mm cut, although it also shows a very good agreement, is not recommended, as well as all the cuts with length comparable or larger than voxel dimensions, as a general rule to ensure a adequate spatial sampling with respect to the resolution of the image used; in addition the simulation time reduction using larger cuts with respect to 0.1 mm or 0.5 mm is minimal.

The combination of parameters giving the fastest simulation among the examined ones is R64 resampling with 4.0 mm cut range, reducing the simulation time to about a fourth of the reference simulation time. As discussed just above, a smaller cut would be in any case suggested, with a length of at least half the size of the voxel (3.58 mm of side in axial direction for R64 resampling); a cut with length between 0.5 and 1.5 mm would in any case give a excellent time reduction, between 30% and 25% of the original computation time. Using R64 resampling returns less accuracy with respect to R8 resampling, but its level of accuracy can be considered still acceptable, especially for liver-related VOIs, with an agreement in terms of ε within 6% in healthy liver perfused and within 3% in all the other liver-related VOIs.

Finally it is worth mentioning the parameter combination using RS resampling and 0.5 mm cut, which enables a time reduction to about 40% of reference time while ensuring fair

agreement in terms of ε, within 4% in healthy liver and within 1% in all the other liver-related VOIs. This type of resampling, producing a CT matching with the spatial resolution and dimensions the SPECT, obviously causes a loss of resolution in comparison to the N CT. Nevertheless, this approach presents some positive aspects, such as an easier management of volume translations in the GATE geometry (*GATE's Documentation* 2021) and a reduction of the complexity for logical operations involving images obtained from different modalities (PET, SPECT, CT, etc.) (Pistone *et al.* 2020), without introducing further interpolations between voxels, since CT and SPECT voxels are in one-to-one correspondence with this kind of resampling. The observed deviations of faster calculation results with respect to the reference values, ε, should be compared with the levels of accuracy of external beam radiotherapy ($\pm$5%) and the broader levels of uncertainty acceptable in internal dosimetry (generally, $\pm$10%) (Pereira *et al.* 2010). The choice of a range cut of 0.1 mm and of the R8 resampling, which considering the native resolution of the employed CT image, produced an image with voxel dimensions of about $1.8\times1.8\times4.0$ mm^3, emerged as the optimal compromise between CT resolution and cuts for the examined patient case; further studies on a wider number of patients could confirm the general reliability of this result.

4. Conclusions

The influence on simulation times and on dosimetric accuracy of CT resampling and of production cuts on secondary particles in GATE MC simulations for a case of ^{90}Y TARE patient-specific voxel dosimetry was investigated. From the results emerged that reducing the CT resolution down to values comparable to the ones of SPECT, together with adopting production cuts of the order of 0.1-0.5 mm, can reduce computation time down to $\sim$30% of the reference simulation obtained using the native CT image and a production cut of 0.01 mm, without drastically affecting the absorbed dose accuracy. In fact, even with the lowest resolution and the larger cuts employed, average dose relative percent differences with reference simulation was within 6% in liver-related VOIs, 14% in lungs and 4% in kidneys. The optimal combination of parameters, ensuring dosimetric agreement within 1% in liver-related VOIs, within 5% in lungs and within 2% in kidneys, while reducing simulation time down to $\sim$45%, results to be CT resampling with voxel volume 8 times larger than the native one and production cut between 0.1 and 0.5 mm. The use of a CT resampling having the same resolution and volume of SPECT scan shows acceptable agreement with reference too, and time saving of $\sim$40%, appearing therefore as another promising choice. The analysis of a single patient case allowed us to identify a reliable procedure of optimization of MC computing efficiency in voxel dosimetry of ^{90}Y TARE treatments. Future more extensive studies on a wider set of cases could better confirm the obtained evidences, and highlight eventual different findings regarding dose accuracy, in particular for patients exhibiting peculiar microspheres distribution in the liver, such as cases of "super-selective" treatments on one side, or lobar/whole organ treatments on the other one.

References

3D Slicer Image Computing Platform (2021). URL: https://www.slicer.org/ (visited on 04/15/2021).

3D Slicer User Manual Documentation (2021). URL: https://www.slicer.org/wiki/Documentation/4.10 (visited on 04/15/2021).

GATE's Documentation (2021). URL: https://opengate.readthedocs.io/en/latest/ (visited on 04/15/2021).

Geant4 Book for Application Developers (2021). URL: https://geant4-userdoc.web.cern.ch/UsersGuides/ForApplicationDeveloper/BackupVersions/V10.5-2.0/html/index.html (visited on 04/15/2021).

Geant4 Physics Reference Manual (2021). URL: https://geant4-userdoc.web.cern.ch/UsersGuides/PhysicsReferenceManual/BackupVersions/V10.5-2.0/html/index.html (visited on 04/15/2021).

Agostinelli, S., Allison, J., Amako, K., *et al.* (2003). "Geant4 - a simulation toolkit". *Nuclear Instruments and Methods in Physics Research Section A: Accelerators, Spectrometers, Detectors and Associated Equipment* **506**(3), 250–303. DOI: 10.1016/S0168-9002(03)01368-8.

Ai-dong, W., Yi-can, W., Sheng-xiang, T., and Jiang-hui, Z. (2005). "Effect of CT Image-Based Voxel Size On Monte Carlo Dose Calculation". In: *2005 IEEE Engineering in Medicine and Biology 27th Annual Conference*, pp. 6449–6451. DOI: 10.1109/IEMBS.2005.1615975.

Allison, J. *et al.* (2016). "Recent developments in Geant4". *Nuclear Instruments and Methods in Physics Research Section A: Accelerators, Spectrometers, Detectors and Associated Equipment* **835**, 186–225. DOI: 10.1016/j.nima.2016.06.125.

Amako, K., Guatelli, S., Ivanchencko, V., Maire, M., Mascialino, B., Murakami, K., Pandola, L., Parlati, S., Pia, M. G., Piergentili, M., Sasaki, T., and Urban, L. (2006). "Geant4 and its validation". *Nuclear Physics B - Proceedings Supplements* **150**, 44–49. DOI: 10.1016/j.nuclphysbps.2004.10.083.

Amato, E., Cicone, F., Auditore, L., Baldari, S., Prior, J. O., and Gnesin, S. (2018). "A Monte Carlo model for the internal dosimetry of choroid plexuses in nuclear medicine procedures". *Physica Medica* **49**, 52–57. DOI: 10.1016/j.ejmp.2018.05.005.

Auditore, L., Amato, E., Italiano, A., Arce, P., Campennì, A., and Baldari, S. (2019). "Internal dosimetry for TARE therapies by means of GAMOS Monte Carlo simulations". *Physica Medica* **64**, 245–251. DOI: 10.1016/j.ejmp.2019.07.024.

Auditore, L., Amato, E., Boughdad, S., Meyer, M., Testart, N., Cicone, F., Beigelman-Aubry, C., Prior, J. O., Schaefer, N., and Gnesin, S. (2020). "Monte Carlo ^{90}Y PET/CT dosimetry of unexpected focal radiation-induced lung damage after hepatic radioembolisation". *Physics in Medicine & Biology* **65**, 235014. DOI: 10.1088/1361-6560/abbc80.

Chiesa, C., Mira, M., Maccauro, M., *et al.* (2015). "Radioembolization of hepatocarcinoma with ^{90}Y glass microspheres: development of an individualized treatment planning strategy based on dosimetry and radiobiology". *European Journal of Nuclear Medicine and Molecular Imaging* **42**(11), 1718–1738. DOI: 10.1007/s00259-015-3068-8.

Dewaraja, Y. K., Frey, E. C., Sgouros, G., Brill, A. B., Roberson, P., Zanzonico, P. B., and Ljungberg, M. (2012). "MIRD pamphlet No. 23: quantitative SPECT for patient-specific 3-dimensional dosimetry in internal radionuclide therapy". *Journal of Nuclear Medicine* **53**(8), 1310–1325. DOI: 10.2967/jnumed.111.100123.

Garin, E., Tselikas, L., Guiu, B., *et al.* (2020). "Personalised versus standard dosimetry approach of selective internal radiation therapy in patients with locally advanced hepatocellular carcinoma (DOSISPHERE-01): a randomised, multicentre, open-label phase 2 trial". *The Lancet Gastroenterology & Hepatology* **6**(1), 17–29. DOI: 10.1016/S2468-1253(20)30290-9.

Gnesin, S., Canetti, L., Adib, S., Cherbuin, N., Silva-Monteiro, M., Bize, P., Denys, A., Prior, J., Baechler, S., and Boubaker, A. (2016). "Partition Model-Based ^{99m}Tc-MAA SPECT/CT Predictive

Dosimetry Compared with ^{99}Y TOF PET/CT Posttreatment Dosimetry in Radioembolization of Hepatocellular Carcinoma: A Quantitative Agreement Comparison". *Journal of Nuclear Medicine* **57**(11), 1672–1678. DOI: 10.2967/jnumed.116.173104.

Huizing, D. M. V., de Wit-van der Veen, B. J., Verheij, M., and Stokkel, M. P. M. (2018). "Dosimetry methods and clinical applications in peptide receptor radionuclide therapy for neuroendocrine tumours: a literature review". *European Journal of Nuclear Medicine and Molecular Imaging* **8**(1), 89. DOI: 10.1186/s13550-018-0443-z.

Jan, S., Santin, G., Strul, D., *et al.* (2004). "GATE: a simulation toolkit for PET and SPECT". *Physics in Medicine & Biology* **49**(19), 4543–4561. DOI: 10.1088/0031-9155/49/19/007.

Kikinis, R., Pieper, S. D., and Vosburgh, K. G. (2014). "3D Slicer: A Platform for Subject-Specific Image Analysis, Visualization, and Clinical Support". In: *Intraoperative Imaging and Image-Guided Therapy*. Ed. by F. A. Jolesz. New York, NY (USA): Springer, pp. 277–289. DOI: 10.1007/978-1-4614-7657-3_19.

Milano, A., Gil, A. V., Fabrizi, E., Cremonesi, M., Veronese, I., Gallo, S., Lanconelli, N., Faccini, R., and Pacilio, M. (2021). "In silico validation of MCID platform for Monte Carlo-based voxel dosimetry applied to 90Y-radioembolization of liver malignancies". *Applied Sciences* **11**(4), 2076–3417. DOI: 10.3390/app11041939.

Moraes, T., Amorim, P., Da Silva, J. V., and Pedrini, H. (2019). "Medical image interpolation based on 3D Lanczos filtering". *Computer Methods in Biomechanics and Biomedical Engineering: Imaging & Visualization* **8**(3), 294–300. DOI: 10.1080/21681163.2019.1683469.

Pereira, J. M., Stabin, M. G., Lima, F. R. A., Guimarães, M. I. C. C., and Forrester, J. W. (2010). "Image Quantification for Radiation Dose Calculations – Limitations and Uncertainties". *Health Physics* **99**(5), 688–701. DOI: 10.1097/HP.0b013e3181e28cdb.

Pistone, D., Auditore, L., Italiano, A., Mandaglio, G., Minutoli, F., Baldari, S., and Amato, E. (2020). "Monte Carlo based dose-rate assessment in 18F-choline PET examination: A comparison between GATE and GAMOS codes". *AAPP Atti della Accademia Peloritana dei Pericolanti. Classe di Scienze Fisiche, Matematiche e Naturali* **98**(1), A5 [15 pages]. DOI: 10.1478/AAPP.981A5.

Richetta, E., Pasquino, M., Poli, M., Cutaia, C., Valero, C., Tabone, M., Peiretti Paradisi, B., Pacilio, M., Pellerito, R. E., and Stasi, M. (2019). "PET-CT post therapy dosimetry in radioembolization with resin 90Y microspheres: Comparison with pre-treatment SPECT-CT 99mTc-MAA results". *Physica Medica* **64**, 16–23. DOI: 10.1016/j.ejmp.2019.05.025.

Sarrut, D., Bardiès, M., Boussion, N., Freud, N., Jan, S., Létang, J.-M., Loudos, G., Maigne, L., Marcatili, S., Mauxion, T., Papadimitroulas, P., Perrot, Y., Pietrzyk, U., Robert, C., Schaart, D. R., Visvikis, D., and Buvat, I. (2014). "A review of the use and potential of the GATE Monte Carlo simulation code for radiation therapy and dosimetry applications". *Medical Physics* **41** (6Part1), 064301. DOI: 10.1118/1.4871617.

Schneider, U., Pedroni, E., and Lomax, A. (1996). "The calibration of CT Hounsfield units for radiotherapy treatment planning". *Physics in Medicine & Biology* **41**(1), 111–124. DOI: 10.1088/0031-9155/41/1/009.

Stokke, C., Gabiña, P. M., Solný, P., Cicone, F., Sandström, M., Gleisner, K. S., Chiesa, C., Spezi, E., Paphiti, M., Konijnenberg, M., Aldridge, M., Tipping, J., Wissmeyer, M., Brans, B., Bacher, K., Kobe, C., and Flux, G. (2017). "Dosimetry-based treatment planning for molecular radiotherapy: a summary of the 2017 report from the Internal Dosimetry Task Force". *European Journal of Nuclear Medicine and Molecular Imaging Physics* **4**, 27. DOI: 10.1186/s40658-017-0194-3.

Strigari, L., Konijnenberg, M., Chiesa, C., Bardies, M., Du, Y., Gleisner, K. S., Lassmann, M., and Flux, G. (2014). "The evidence base for the use of internal dosimetry in the clinical practice of molecular radiotherapy". *European Journal of Nuclear Medicine and Molecular Imaging* **41**, 1976–1988. DOI: 10.1007/s00259-014-2824-5.

Tsougos, I., Loudos, G., Georgoulias, P., Theodorou, K., and Kappas, C. (2010). "Patient-specific internal radionuclide dosimetry". *Nuclear Medicine Communications* **31**(2), 97–106. DOI: 10.1097/MNM.0b013e328330626f.

Ziegenhein, P., Pirner, S., Kamerling, C. P., and Oelfke, U. (2015). "Fast CPU-based Monte Carlo simulation for radiotherapy dose calculation". *Physics in Medicine & Biology* **60**(15), 6097. DOI: 10.1088/0031-9155/60/15/6097.

Annex

TABLE A1. VOI volumes (cm^3) for each CT resampling.

VOI	Li.	Le.	Li.P.	H.Li.	H.Li.P.	R.K.	L.K.	R.L.	L.L.
CT									
N	2770.24	359.53	892.59	2415.99	533.06	198.97	262.74	404.83	652.36
R2	2773.69	360.73	893.52	2418.72	532.79	197.94	262.85	400.88	647.72
R8	2770.23	359.53	892.59	2415.98	533.06	198.86	262.74	404.87	652.36
R64	2735.02	355.95	883.36	2383.03	527.41	201.83	262.55	377.57	627.91
RS	2767.86	358.47	893.14	2415.14	534.67	198.47	262.43	408.89	654.46

TABLE A2. $\langle D \rangle$ (Gy), $\langle \delta \rangle$ (%) and ε (%) (Eq. 5) for N CT in the considered VOIs, respectively reported as the upper, middle and lower value in column for each box, *i.e.*, for each combination of range cut and VOI.

	VOI	Li.	Le.	Li.P.	H.Li.	H.Li.P.	R.K.	L.K.	R.L.	L.L.
CT	**Cut**									
N	0.01	31.032	168.844	104.761	11.914	61.540	0.6476	0.3219	6.084	1.501
		22.466	2.500	3.550	25.394	4.259	42.075	63.671	17.108	40.927
		/	/	/	/	/	/	/	/	/
	0.05	32.032	168.850	104.765	11.912	61.543	0.6489	0.3229	6.063	1.501
		22.436	2.498	3.548	25.360	4.256	41.958	63.570	17.111	40.997
		-1.81E-05	3.43E-05	3.56E-05	-1.25E-04	4.04E-05	1.94E-03	3.29E-03	-3.53E-03	-5.32E-04
	0.1	32.033	168.860	104.751	11.912	61.512	0.6497	0.3235	6.0017	1.491
		22.448	2.498	3.549	25.374	4.258	41.992	63.522	17.234	41.074
		2.46E-05	9.32E-05	-9.88E-05	-1.43E-04	-4.58E-04	3.29E-03	4.95E-03	-1.36E-02	-7.08E-03
	0.5	32.032	168.836	104.748	11.914	61.523	0.6498	0.3213	5.958	1.485
		22.522	2.507	3.561	25.457	4.272	42.157	63.828	17.290	41.092
		-1.29E-06	-4.66E-05	-1.27E-04	4.87E-05	-2.76E-04	3.36E-03	-1.94E-03	-2.08E-02	-1.10E-02
	1.0	32.032	168.852	104.745	11.912	61.507	0.6505	0.3240	5.9674	1.4849
		22.588	2.517	3.576	25.532	4.290	42.075	63.826	17.491	41.439
		-1.03E-05	4.91E-05	-1.62E-04	-1.53E-04	-5.52E-04	4.46E-03	6.14E-03	-1.92E-02	-1.10E-02

TABLE A3. $\langle D \rangle$ (Gy), $\langle \delta \rangle$ (%) and ε (%) (Eq. 5) for R2 CT in the considered VOIs, respectively reported as the upper, middle and lower value in column for each box, *i.e.*, for each combination of range cut and VOI.

	VOI	Li.	Le.	Li.P.	H.Li.	H.Li.P.	R.K.	L.K.	R.L.	L.L.
CT	**Cut**									
R2	0.01	32.054	167.762	104.999	11.814	61.715	0.6481	0.3247	5.843	1.449
		16.530	1.842	2.603	18.716	3.128	30.782	52.228	12.985	33.527
		6.59E-04	-6.41E-03	2.27E-03	-8.40E-03	2.83E-03	7.55E-04	8.68E-03	-3.97E-02	-3.53E-02
	0.05	32.051	167.738	104.988	11.814	61.712	0.6506	0.3242	5.846	1.446
		16.520	1.840	2.601	18.704	3.125	30.689	52.264	12.962	33.482
		5.62E-04	-6.55E-03	2.16E-03	-8.38E-03	2.79E-03	4.70E-03	6.95E-03	-3.92E-02	-3.69E-02
	0.1	32.052	167.760	104.986	11.813	61.692	0.6525	0.3225	5.825	1.433
		16.510	1.840	2.601	18.693	3.126	30.675	52.276	12.991	33.574
		6.18E-04	-6.42E-03	2.14E-03	-8.48E-03	2.47E-03	7.63E-03	1.79E-03	-4.26E-02	-4.54E-02
	0.5	32.051	167.736	104.992	11.814	61.720	0.6521	0.3232	5.786	1.428
		16.570	1.844	2.606	18.761	3.132	30.736	52.317	13.008	33.752
		5.56E-04	-6.56E-03	2.20E-03	-8.42E-03	2.91E-03	6.95E-03	4.15E-03	-4.91E-02	-4.88E-02
	1.5	32.050	167.744	104.979	11.812	61.692	0.6511	0.3245	5.759	1.430
		16.618	1.852	2.619	18.814	3.147	30.872	52.370	13.227	33.922
		5.39E-04	-6.51E-03	2.07E-03	-8.53E-03	2.46E-03	5.41E-03	7.96E-03	-5.36E-02	-4.78E-02

TABLE A4. $\langle D \rangle$ (Gy), $\langle \delta \rangle$ (%) and ε (%) (Eq. 5) for R8 CT in the considered VOIs, respectively reported as the upper, middle and lower value in column for each box, *i.e.*, for each combination of range cut and VOI.

	VOI	Li.	Le.	Li.P.	H.Li.	H.Li.P.	R.K.	L.K.	R.L.	L.L.
CT	**Cut**									
R8	0.01	31.907	168.390	104.693	11.813	61.696	0.6511	0.3282	5.841	1.458
		10.555	1.170	1.662	11.930	1.994	19.348	37.034	8.452	22.390
		-3.91E-03	-2.69E-03	-6.52E-04	-8.47E-03	2.52E-03	5.37E-03	1.96E-02	-3.99E-02	-2.92E-02
	0.05	31.909	168.389	104.685	11.814	61.696	0.6469	0.3269	5.840	1.456
		10.542	1.169	1.660	11.916	1.992	19.385	37.096	8.429	22.372
		-3.85E-03	-2.69E-03	-6.56E-04	-8.28E-03	2.52E-03	-1.14E-03	1.56E-02	-4.02E-02	-2.99E-02
	0.1	31.906	168.375	104.685	11.814	61.693	0.6481	0.3277	5.816	1.450
		10.540	1.169	1.660	11.913	1.992	19.384	36.853	8.461	22.470
		-3.95E-03	-2.78E-03	-7.27E-04	-8.38E-03	2.48E-03	7.48E-04	1.80E-02	-4.41E-02	-3.40E-02
	0.5	31.905	138.379	104.679	11.812	61.680	0.6478	0.3271	5.777	1.444
		10.552	1.170	1.662	11.926	1.994	19.371	36.991	8.469	22.417
		-3.98E-03	-2.75E-03	-7.87E-04	-8.54E-03	2.26E-03	3.33E-04	1.63E-02	-5.06E-02	-3.79E-02
	2.0	31.907	168.395	104.682	11.812	61.673	0.6510	0.3287	5.744	1.436
		10.568	1.174	1.667	11.944	2.001	19.446	37.139	8.585	22.541
		-3.91E-03	-2.66E-03	-7.63E-04	-8.53E-03	2.15E-03	5.30E-03	2.11E-02	-5.60E-02	-4.36E-02

TABLE A5. $\langle D \rangle$ (Gy), $\langle \delta \rangle$ (%) and ε (%) (Eq. 5) for R64 CT in the considered VOIs, respectively reported as the upper, middle and lower value in column for each box, *i.e.*, for each combination of range cut and VOI.

	VOI	Li.	Le.	Li.P.	H.Li.	H.Li.P.	R.K.	L.K.	R.L.	L.L.
CT	**Cut**									
R64	0.01	31.635	164.539	105.779	12.141	64.918	0.6406	0.3301	5.331	1.367
		4.583	0.527	0.735	5.176	0.879	8.478	16.708	4.236	11.708
		-1.24E-02	-2.55E-02	9.71E-03	1.91E-02	5.49E-02	-1.08E-02	2.54E-02	-1.24E-01	-8.98E-02
	0.05	31.634	164.520	105.772	12.142	64.920	0.6395	0.3327	5.345	1.375
		4.582	0.526	0.734	5.175	0.878	8.486	16.722	4.234	11.735
		-1.24E-02	-2.56E-02	9.65E-03	1.91E-02	5.49E-02	-1.25E-02	3.35E-02	-1.22E-01	-8.40E-02
	0.1	31.631	164.528	105.771	12.138	64.912	0.6391	0.3308	5.340	1.371
		4.582	0.526	0.734	5.175	0.878	8.483	16.612	4.226	11.663
		-1.25E-02	-2.56E-02	9.63E-03	1.88E-02	5.48E-02	-1.32E-02	2.77E-02	-1.23E-01	-8.71E-02
	0.5	31.631	164.514	105.758	12.140	64.900	0.6407	0.3322	5.314	1.362
		4.589	0.526	0.734	5.182	0.878	8.465	16.604	4.217	11.715
		-1.25E-02	-2.56E-02	9.51E-03	1.90E-02	5.46E-02	-1.07E-02	3.19E-029	-1.27E-01	-9.28E-02
	4.0	31.633	164.532	105.760	12.139	64.891	0.642	0.332	5.263	1.360
		4.593	0.527	0.735	5.188	0.880	8.485	16.654	4.269	8.484
		-1.25E-02	-2.55E-02	9.53E-03	1.89E-02	5.44E-02	-8.21E-03	3.08E-02	-1.35E-01	-9.44E-02

TABLE A6. $\langle D \rangle$ (Gy), $\langle \delta \rangle$ (%) and ε (%) (Eq. 5) for RS CT in the considered VOIs, respectively reported as the upper, middle and lower value in column for each box, *i.e.*, for each combination of range cut and VOI.

	VOI	Li.	Le.	Li.P.	H.Li.	H.Li.P.	R.K.	L.K.	R.L.	L.L.
CT	**Cut**									
RS	0.01	31.956	169.278	105.165	11.510	61.618	0.6497	0.3235	5.613	1.349
		4.858	0.530	0.752	5.502	0.903	8.887	18.333	4.289	12.823
		-2.39E-03	2.57E-03	3.85E-03	-3.39E-02	1.26E-03	3.24E-03	4.82E-03	-7.75E-02	-1.02E-01
	0.05	31.954	169.270	105.155	11.509	61.607	0.6505	0.3240	5.607	1.352
		4.846	0.529	0.751	5.490	0.902	8.863	18.094	4.283	12.786
		-2.44E-03	2.52E-03	3.76E-03	-3.39E-02	1.08E-03	4.48E-03	6.45E-03	-7.85E-02	-9.98E-02
	0.1	31.953	169.266	105.147	11.509	61.596	0.6521	0.3238	5.598	1.348
		4.848	0.529	0.751	5.491	0.902	8.883	18.256	4.287	12.787
		-2.47E-03	2.50E-03	3.68E-03	-3.40E-02	9.02E-04	6.88E-03	5.72E-03	-8.00E-02	-1.02E-01
	0.5	31.954	169.265	105.153	11.510	61.607	0.6537	0.3234	5.673	1.344
		4.847	0.529	0.751	5.490	0.902	8.849	18.430	4.286	12.616
		-2.45E-03	2.49E-03	3.74E-03	-3.39E-02	1.08E-03	9.45E-03	7.44E-03	-8.41E-02	-1.05E-01
	4.0	31.953	169.278	105.150	11.507	61.592	0.6471	0.3225	5.45	1.335
		4.858	0.530	0.752	5.502	0.903	8.998	18.441	4.336	12.730
		-2.47E-03	2.57E-03	3.71E-03	-3.41E-02	8.48E-04	-7.80E-04	1.87E-03	-8.87E-02	-1.11E-01

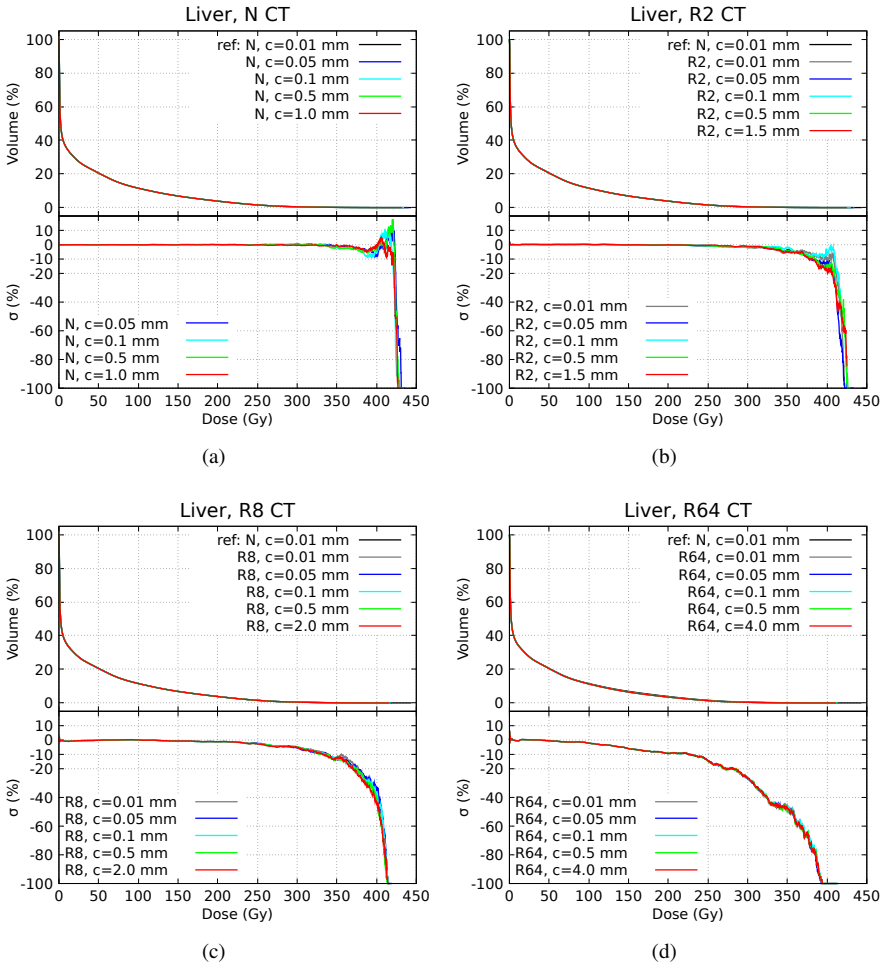

FIGURE A1. DVHs and σ's (%) in VOIs

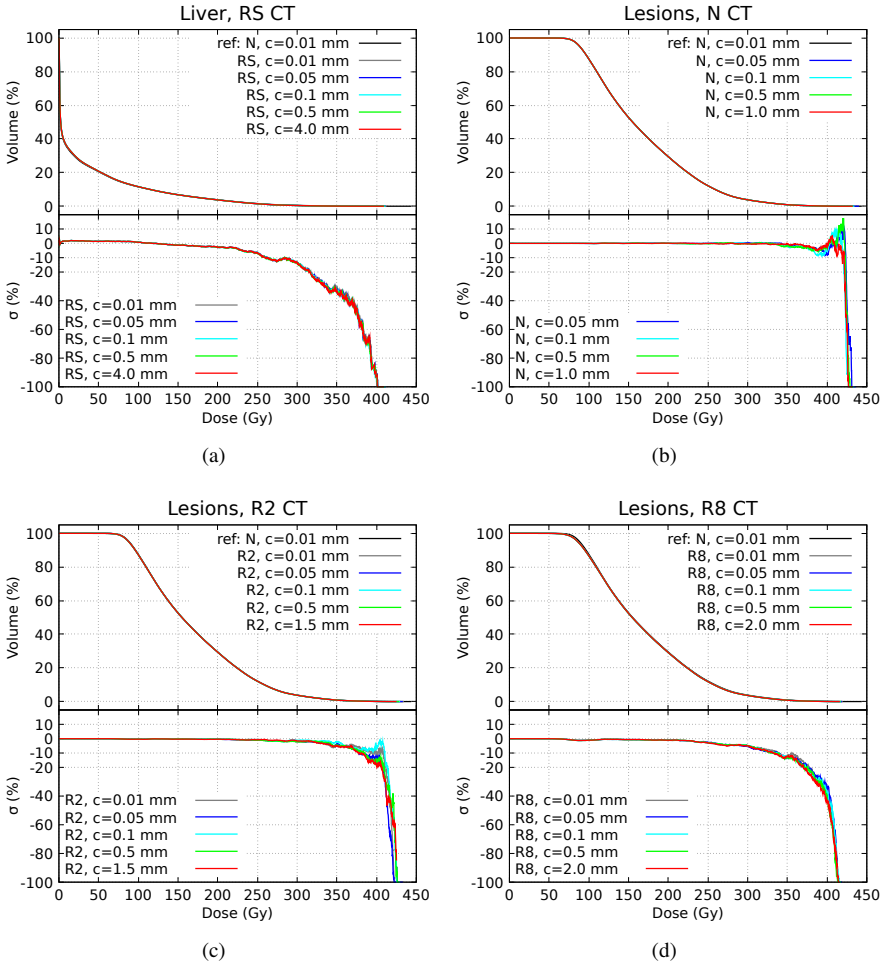

FIGURE A2. DVHs and σ's (%) in VOIs

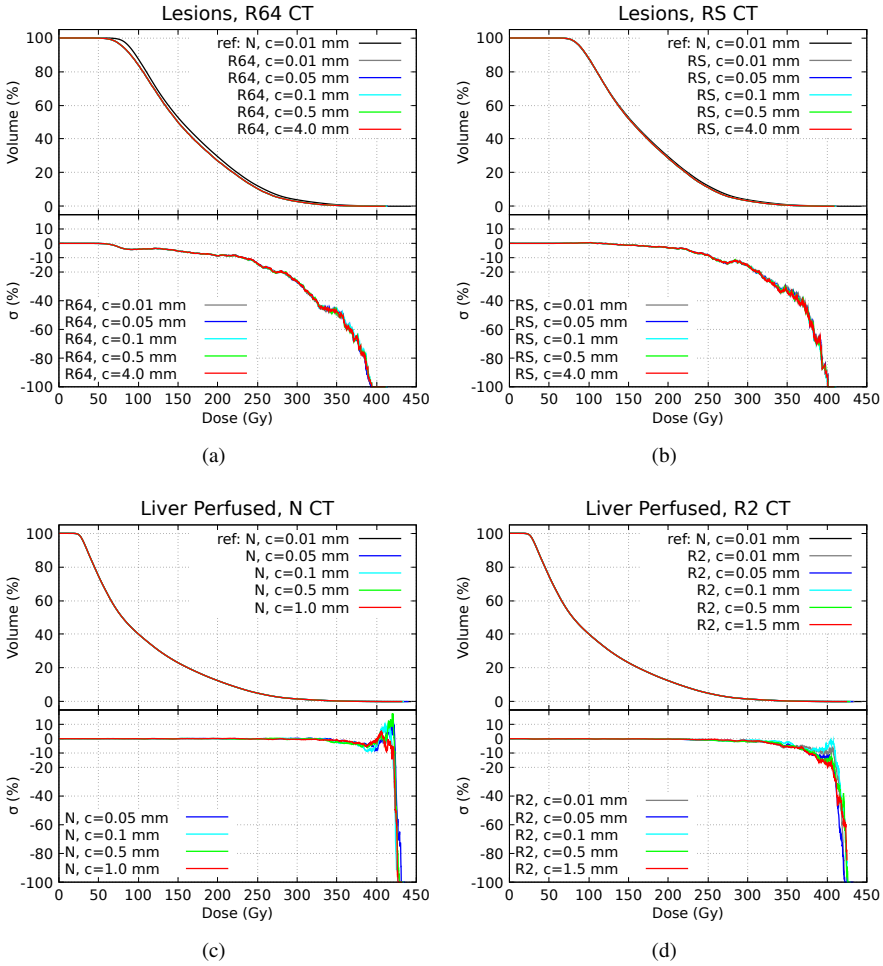

FIGURE A3. DVHs and σ's (%) in VOIs

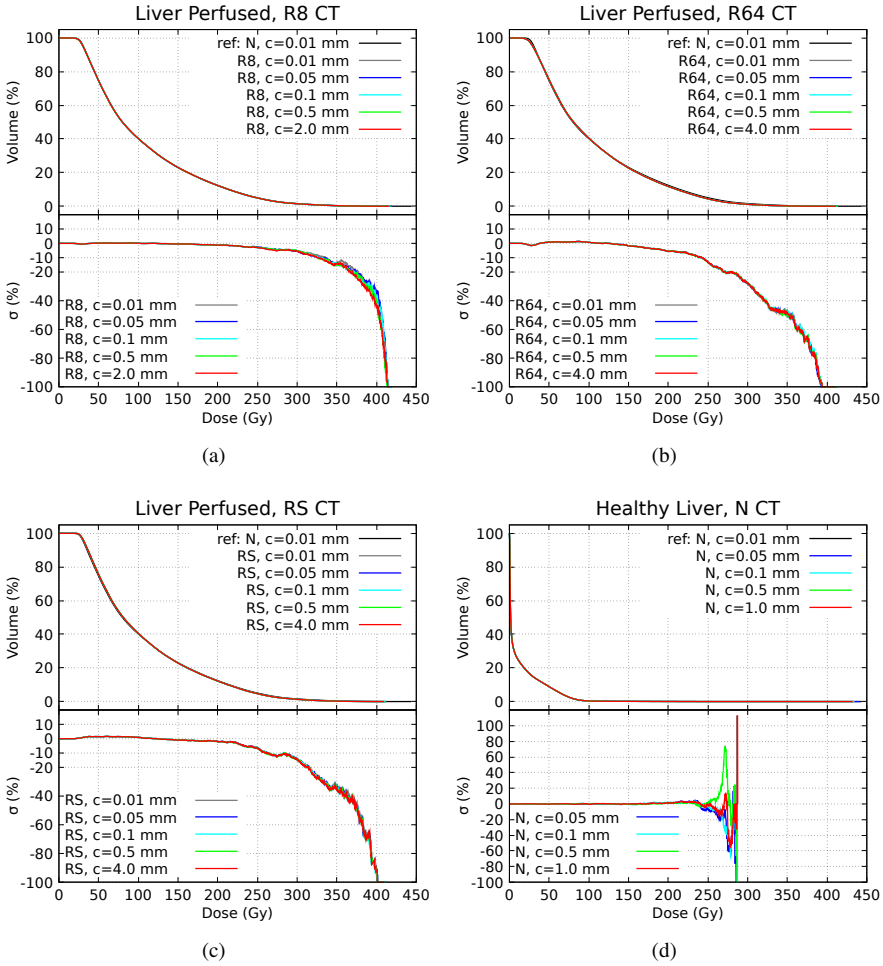

FIGURE A4. DVHs and σ's (%) in VOIs

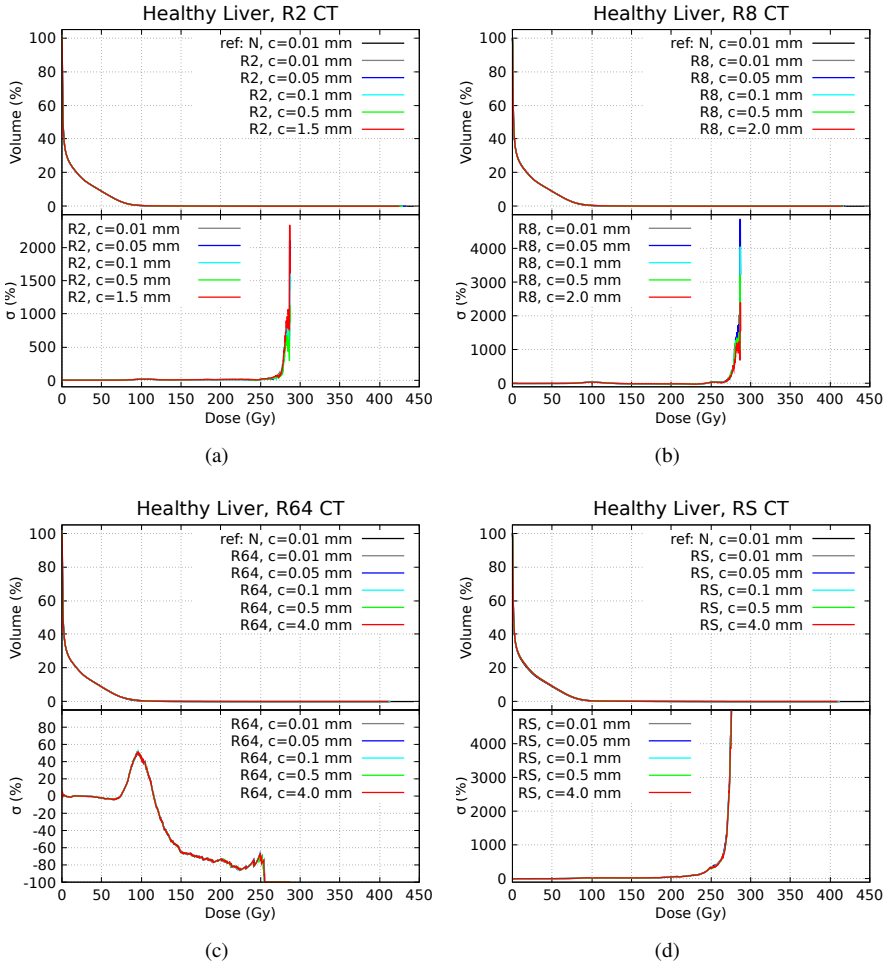

FIGURE A5. DVHs and σ's (%) in VOIs

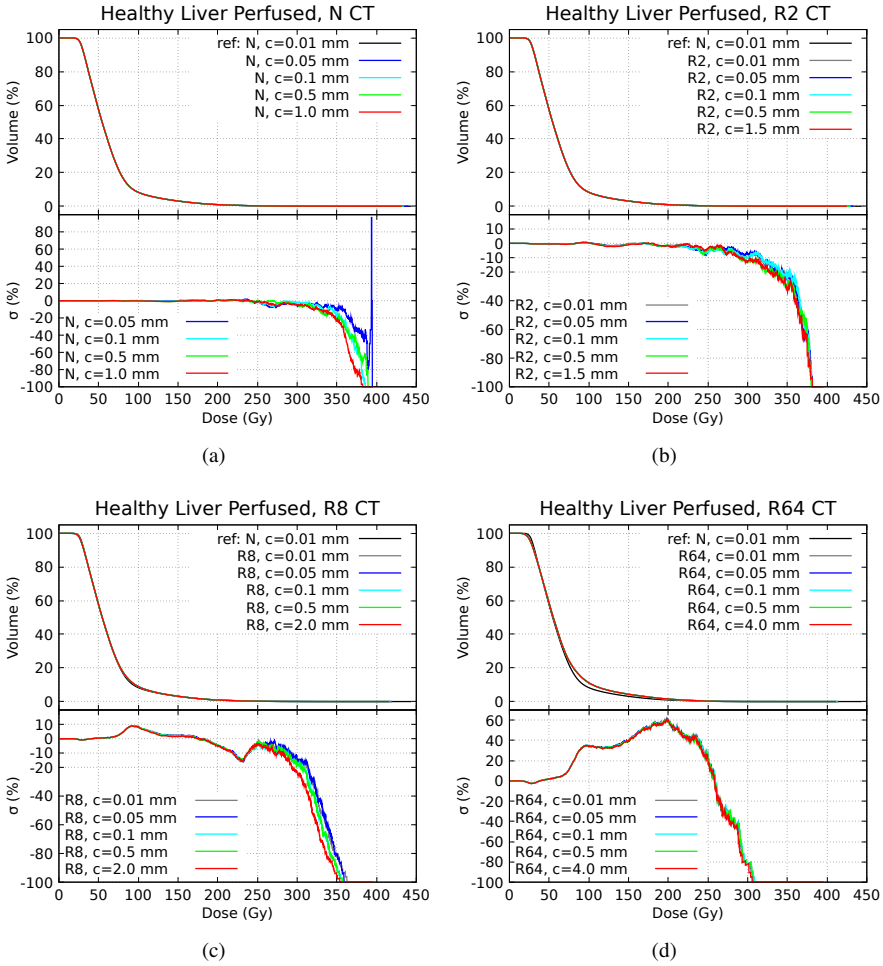

FIGURE A6. DVHs and σ's (%) in VOIs

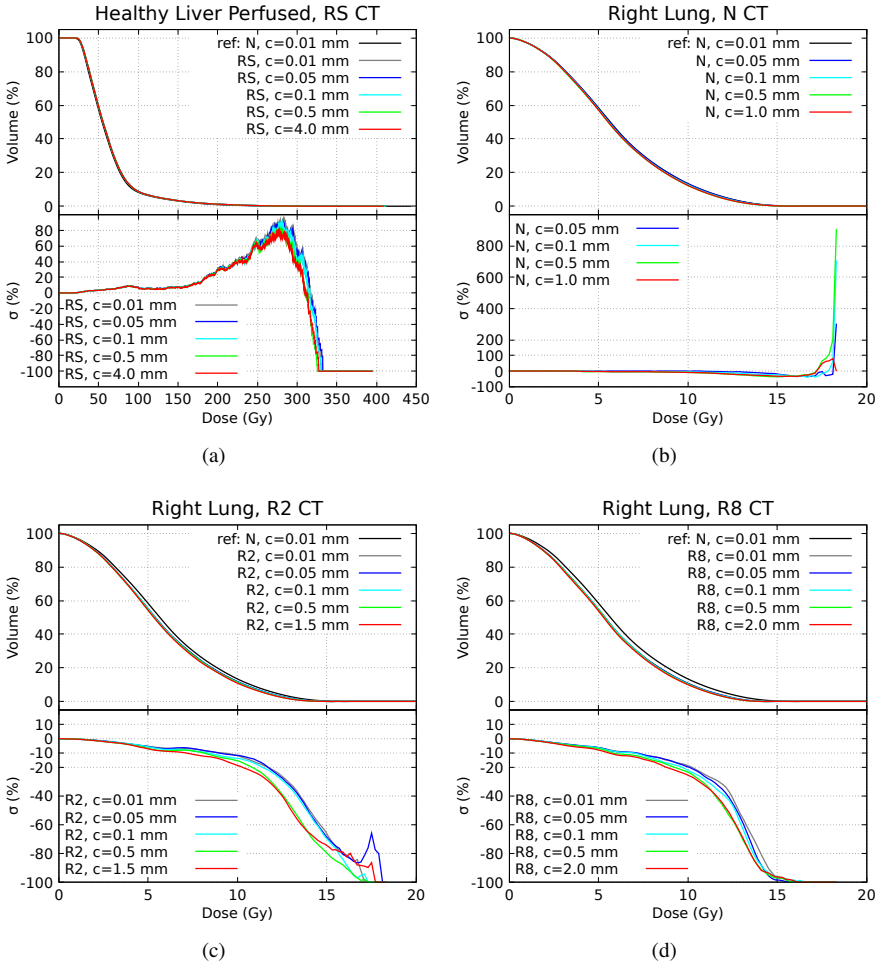

FIGURE A7. DVHs and σ's (%) in VOIs

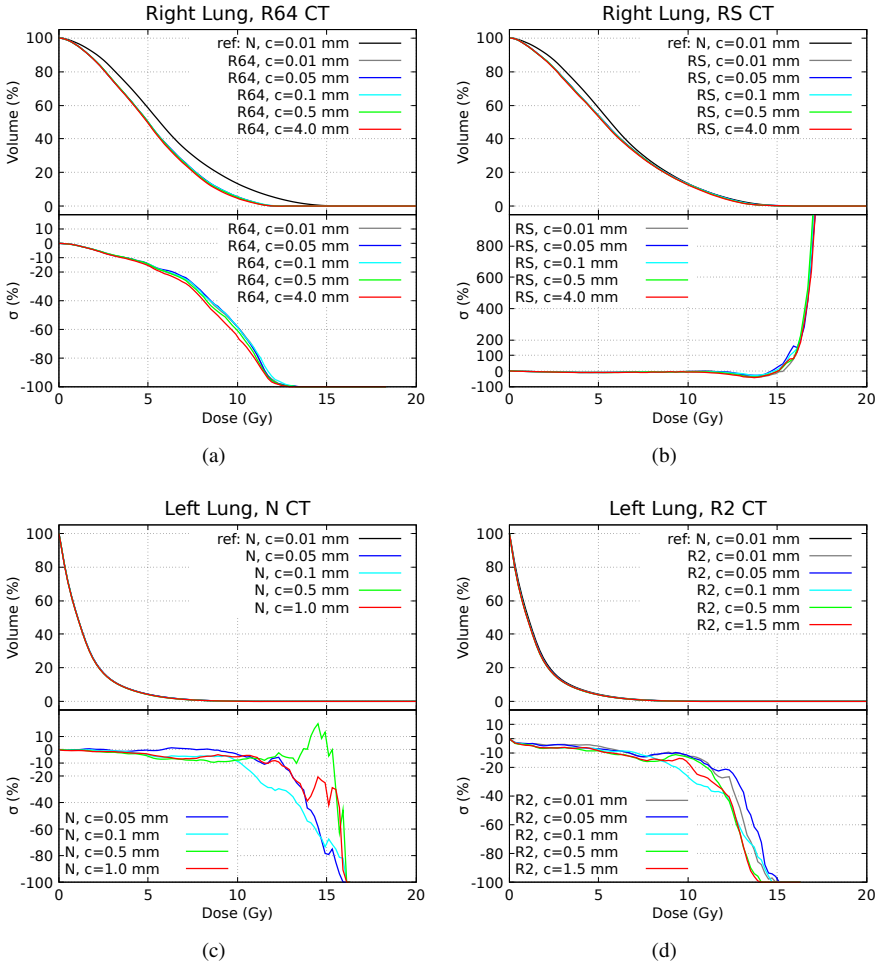

FIGURE A8. DVHs and σ's (%) in VOIs

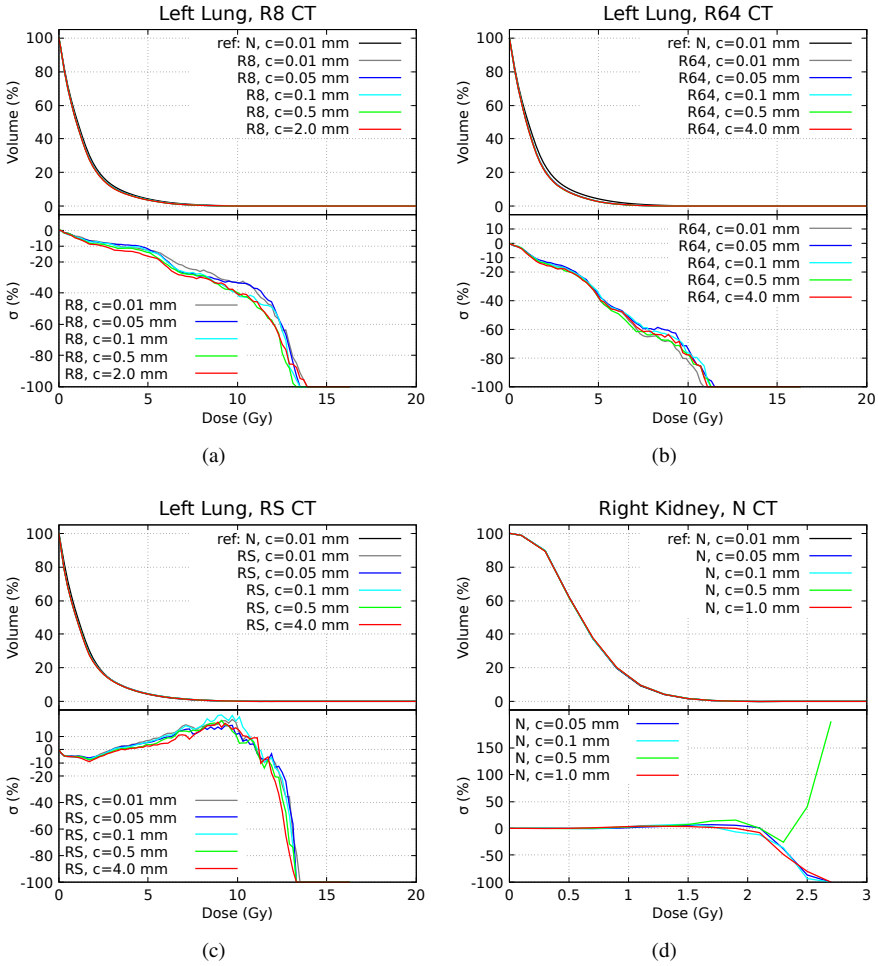

FIGURE A9. DVHs and σ's (%) in VOIs

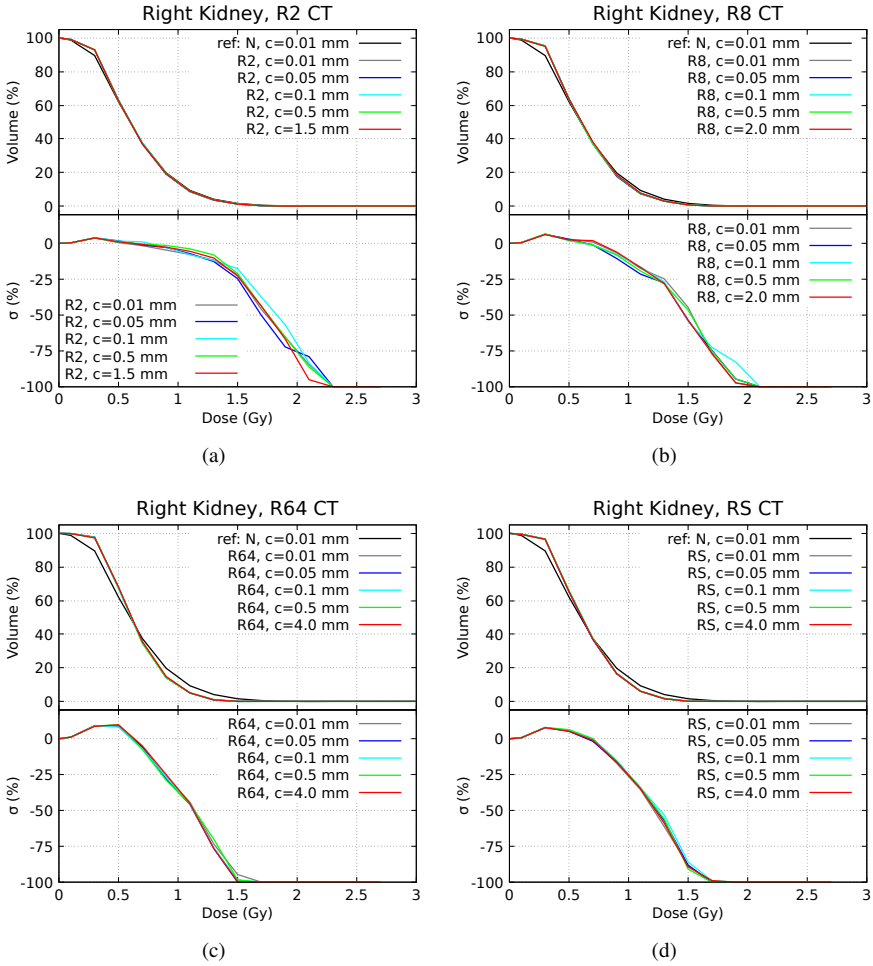

FIGURE A10. DVHs and σ's (%) in VOIs

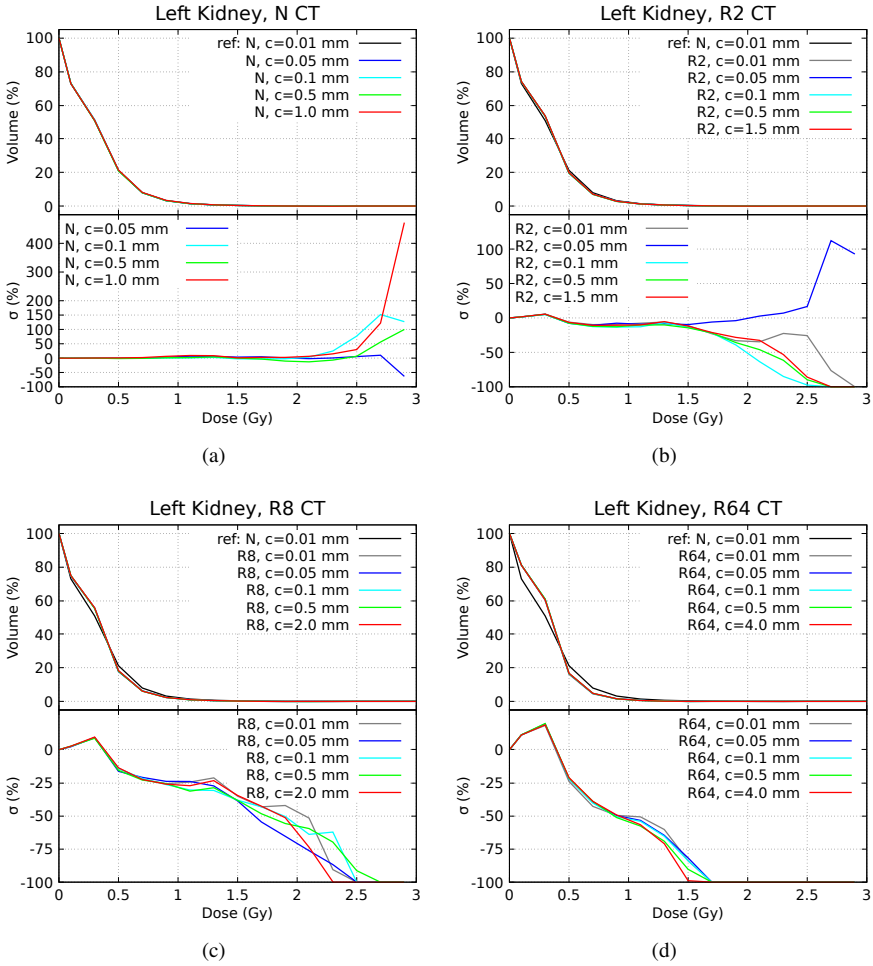

FIGURE A11. DVHs and σ's (%) in VOIs

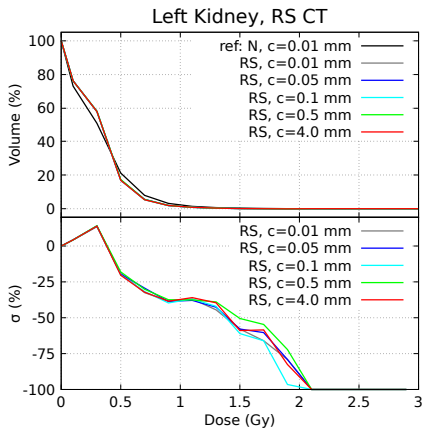

(a)

FIGURE A12. DVHs and σ's (%) in VOIs

[a] Università degli Studi di Messina,
Dipartimento di Scienze Matematiche e Informatiche, Scienze Fisiche e Scienze della Terra,
Contrada Papardo, 98166 Messina, Italy

[b] Istituto Nazionale di Fisica Nucleare,
Sezione di Catania,
Catania, Italy

[c] Università degli Studi di Messina,
Dipartimento di Scienze Biomediche, Odontoiatriche e delle Immagini Morfologiche e Funzionali,
Via Consolare Valeria, 98125 Messina, Italy

[d] Azienda Ospedaliera Universitaria Policlinico "Gaetano Martino",
Unità Operativa Complessa "Medicina Nucleare",
Via Consolare Valeria, 98125 Messina, Italy

[*] To whom correspondence should be addressed | email: italianoa@unime.it

Communicated 26 November 2020; manuscript received 18 May 2021; published online 14 November 2021